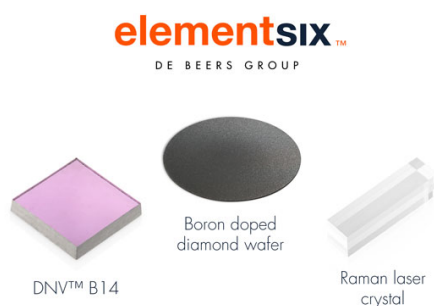


OPEN ACCESS

The LiNiO_2 Cathode Active Material: A Comprehensive Study of Calcination Conditions and their Correlation with Physicochemical Properties. Part I. Structural Chemistry

To cite this article: Philipp Kurzhals *et al* 2021 *J. Electrochem. Soc.* **168** 110518

View the [article online](#) for updates and enhancements.



Element Six is a world leader in the development and production of synthetic diamond solutions






Since 1959, our focus has been on engineering the properties of synthetic diamond to unlock innovative applications, such as thermal management, water treatment, optics, quantum and sensing. Our patented technology places us at the forefront of synthetic diamond innovation, enabling us to deliver competitive advantage to our customers through diamond-enabled solutions.

Find out more and contact the team at:
ustechnologies@e6.com





The LiNiO₂ Cathode Active Material: A Comprehensive Study of Calcination Conditions and their Correlation with Physicochemical Properties. Part I. Structural Chemistry

Philipp Kurzahls,^{1,2,*,z}  Felix Riewald,^{1,3,=}  Matteo Bianchini,^{1,4,*}  Heino Sommer,¹
Hubert A. Gasteiger,^{3,**}  and Jürgen Janek^{2,z,*} 

¹BASF SE, New Battery Materials and Systems, D-67056 Ludwigshafen, Germany

²Institute of Physical Chemistry & Center for Materials Research, Justus Liebig University, D-35392 Giessen, Germany

³Chair of Technical Electrochemistry, Department of Chemistry and Catalysis Research Center, Technical University of Munich, D-85748 Garching, Germany

⁴Battery and Electrochemistry Laboratory (BELLA), Institute of Nanotechnology, Karlsruhe Institute of Technology (KIT), Hermann-von-Helmholtz-Platz 1, 76344 Eggenstein-Leopoldshafen, Germany

Following the demand for increased energy density of lithium-ion batteries, the Ni content of the Nickel-Cobalt-Manganese oxide (NCM) cathode materials has been increased into the direction of LiNiO₂ (LNO), which regained the attention of both industry and academia. To understand the correlations between physicochemical parameters and electrochemical performance of LNO, a calcination study was performed with variation of precursor secondary particle size, maximum calcination temperature and Li stoichiometry. The structural properties of the materials were analyzed by means of powder X-ray diffraction, magnetization measurements and half-cell voltage profiles. All three techniques yield good agreement concerning the quantification of Ni excess in the Li layer (1.6%–3.7%). This study reveals that the number of Li equivalents per Ni is the determining factor concerning the final stoichiometry rather than the calcination temperature within the used calcination parameter space. Contrary to widespread belief, the Ni excess shows no correlation to the 1st cycle capacity loss, which indicates that a formerly overlooked physical property of LNO, namely primary particle morphology, has to be considered.

© 2021 The Author(s). Published on behalf of The Electrochemical Society by IOP Publishing Limited. This is an open access article distributed under the terms of the Creative Commons Attribution 4.0 License (<http://creativecommons.org/licenses/by/4.0/>), which permits unrestricted reuse of the work in any medium, provided the original work is properly cited. [DOI: 10.1149/1945-7111/ac33e5]



Manuscript submitted August 29, 2021; revised manuscript received October 20, 2021. Published November 9, 2021.

The current generation of lithium-ion batteries (LIBs) requires further improvements to ease the commercialization and strengthen the market share of battery electric vehicles (BEVs).^{1–3} While all parts of the battery cells are targeted by researchers, one of the key components under investigation is the cathode active material (CAM), as it is the main cost driver of the overall electrochemical cell and it strongly affects the achievable energy and power density.⁴ Although the interest in olivine LiFePO₄ as low-cost CAM with moderate specific capacity recently has risen and other alternatives such as spinel Li(Mn,Ni)₂O₄ and overlithiated Li-rich and Mn-rich cathodes are currently examined,⁵ the predominant choice of materials are the layered transition metal oxides Li(Ni_{1-x-y}Co_xMn_y)O₂ (NCM) and Li(Ni_{1-x-y}Co_xAl_y)O₂ (NCA). These show a good compromise between high power and high energy density applications at sufficiently low cost and, provided that the Co content is minimized, raw material abundance.⁶ Driven by the requirements of BEV manufacturers for further driving range increase and reduction of costs, the Ni content of these layered transition metal oxides has been increased over the past years and the market share of BEVs using LIBs with Ni contents of 80% and above is expected to significantly increase in the near future.⁷ With increasing Ni fraction in the CAM, the extractable amount of Li increases (and thus, the achievable capacity and resulting energy density at a fixed voltage cut-off), but this comes at the cost of reduced cycling stability.^{8,9} Ni-rich NCM and NCA phases tend to show increased degradation, involving the bulk and most importantly the surface of the CAM. For example, oxygen loss at high degree of delithiation is connected with decomposition of the surface structure (densification towards rock salt-like structure), while large anisotropic crystal lattice changes (total change of unit cell volume during charge of e.g. ~ 5% for Li(Ni_{0.8}Co_{0.1}Mn_{0.1})O₂) eventually lead to particle fracture.^{10–13} Major efforts have been spent to chemical stabilization approaches like bulk substitution with other elements or surface modification in form of thin coatings on the particles.^{14–18} Novel

approaches also involve material modifications to address the fracturing issue by optimizing the particle morphology (single crystal or rather monolithic materials).¹⁹ Moreover, intentional orientation of primary particles in radial direction was introduced to better accommodate the volume changes during cycling. Materials with transition metal concentration gradients were also investigated, which reduce the amount of reactive Ni in contact with the liquid electrolyte.^{20–22}

Unfortunately, in comparison to the originally commercialized layered compound LiCoO₂, NCM- and NCA-type materials suffer from poor 1st cycle coulombic efficiencies, a clear limitation that has to be better understood to fully exploit the potential of this class of cathode active materials.^{23–26} Due to such a 1st cycle capacity loss, not all the deintercalated Li can be reintroduced into the CAM structure during discharge. LiNiO₂ (LNO) as the 100% Ni end member of the NCM and NCA materials is the natural model system to investigate this effect. Early research showed that LNO always tends to be Li deficient and contains an excess of Ni²⁺ (“Ni excess” or “off-stoichiometry”) in the Li layers, despite optimized calcination conditions, leading to a stoichiometry of Li_{1-z}Ni_{1+z}O₂.^{27–29} Incomplete oxidation and deficiency of Li₂O leads to the solid solution of LiNiO₂ (z = 0) and NiO (z = 1), where 2z Ni²⁺ ions are present with half of them located in the Li layer and the other half in the Ni layer. This Ni excess was shown to have a significant impact on physical and electrochemical properties, e.g. on magnetic properties and phase transitions during cycling.³⁰

A commonly found hypothesis throughout the literature is the connection between the poor 1st cycle coulombic efficiency and the excess Ni²⁺ in the Li layers.^{31–33} Numerous reports on the synthesis of near-stoichiometric LNO were published, but the general approach in the literature is to vary one or more calcination parameter(s) in large steps to see clear effects on the resulting physicochemical properties and electrochemical performance.^{27,31,34–36} Unfortunately, this often leads to conclusions that are hard to generalize and could be easily misinterpreted. Furthermore, in industrial optimization processes narrow parameter ranges are considered in contrast to academia, where a more fundamental understanding is intended.

Therefore, the goal of this study is to systematically vary multiple calcination parameters (secondary particle size of hydroxide

^zThese authors contributed equally to this work.

*Electrochemical Society Member.

**Electrochemical Society Fellow.

^zE-mail: philipp.kurzahls@basf.com; juergen.janek@pc.jlug.de

precursor, number of Li equivalents per mole of Ni, maximum calcination temperature) with the aim to prepare $\text{Li}_{1-z}\text{Ni}_{1+z}\text{O}_2$ with minimized z values, and to thoroughly analyze the resulting physicochemical properties. In this first part of the study, synchrotron powder X-ray diffraction (PXRD), measurements of the magnetic properties and 1st cycle voltage profile analysis are performed to properly quantify the stoichiometry of the samples in terms of Ni excess in the Li layers. Afterwards, the obtained values are compared to the 1st cycle capacity loss. In a forthcoming and complementary study, we will investigate the relationship between primary particle morphology, its evolution upon cycling and the electrochemical performance.

Experimental

Calcination of LiNiO_2 .—LNO samples were calcined through a solid-state synthesis route starting from the base materials $\text{Ni}(\text{OH})_2$ and $\text{LiOH}\cdot\text{H}_2\text{O}$. Two commercial batch-type $\text{Ni}(\text{OH})_2$ precursors (Hunan Zoomwe Zhengyuan Advanced Material Trade Co., Ltd.) with two distinct secondary particle sizes (d_{50} values of $(12 \pm 0.5) \mu\text{m}$ and $(4 \pm 0.5) \mu\text{m}$, respectively, Fig. 1c) were utilized, further on referred to as “12 μm precursor” and “4 μm precursor.” $\text{LiOH}\cdot\text{H}_2\text{O}$ was used as Li source (Albemarle Corporation), which was ground prior to the synthesis with an air classifying mill to obtain particles of $\sim 10\text{--}20 \mu\text{m}$. 50 g of $\text{Ni}(\text{OH})_2$ and the respective amount of $\text{LiOH}\cdot\text{H}_2\text{O}$ to get the defined number of Li equivalents per mol of Ni were mixed using a laboratory blender (Kinematica AG). Three different numbers of Li equivalents (0.98, 1.01 and 1.04) were utilized in this study. Afterwards, this premix was filled into a ceramic crucible and fired in a laboratory box-type furnace (Linn High Therm GmbH). An overview of the used calcination conditions and the color and shape coding for the samples used in all figures throughout this study are shown in Fig. 1a. A schematic of the calcination profile is shown in Fig. 1b. First, the temperature was ramped up to 400 °C and fixed for

four hours and then the temperature was ramped up to the respective maximum calcination temperature T_{max} (680 °C, 700 °C and 720 °C, respectively) and was kept for six hours. For both steps a heating rate of $3 \text{ }^\circ\text{C min}^{-1}$ was chosen. This calcination profile was selected to be as close as possible to an industrially feasible process. Thus, a moderate heating ramp and dwell times, that result in an overall calcination time of $\sim 14 \text{ h}$, were chosen. An additional cool-down and grinding step after the 400 °C hold was avoided as this would not be part of industrial practice. All experiments were run in pure oxygen atmosphere (flow rate of 100 liters per hour corresponding to about ten furnace-volume exchanges per hour). After the synthesis the samples were cooled down to 120 °C and brought to a dry room (21 °C, dew point $< -40 \text{ }^\circ\text{C}$) inside a gas-tight box to prevent reactions with ambient moisture and CO_2 . Handling of dry CAM powders was generally done in the dry room. Prior to characterization of the materials and the electrode preparation, the powders were sieved using sieves with a mesh size of 32 μm (Retsch GmbH).

Scanning electron microscopy (SEM) imaging.—A small amount of cathode powder was fixed on a SEM pin holder (Agar Scientific, Ltd.) covered with conducting carbon cement (Plano GmbH). A 6 nm thick platinum layer was added by sputter deposition (SCD 500 Sputter Coater, Bal-Tec AG). Measurements were performed using a SEM with a thermal field emission cathode and an Everhart-Thornley secondary electron detector at an operating voltage of 5 kV (Ultra 55, Carl Zeiss AG).

Powder X-ray diffraction.—Synchrotron powder X-ray diffraction (PXRD) measurements were performed at the ALBA synchrotron. The measurements at ALBA were carried out at the BL04-MSPD beamline³⁷ at a wavelength of $\lambda = 0.62001 \text{ \AA}$ (calibrated using a Si NIST standard) using a Si 111 monochromator and the MYTHEN position sensitive detector in 2θ angular range of $2^\circ\text{--}82^\circ$.

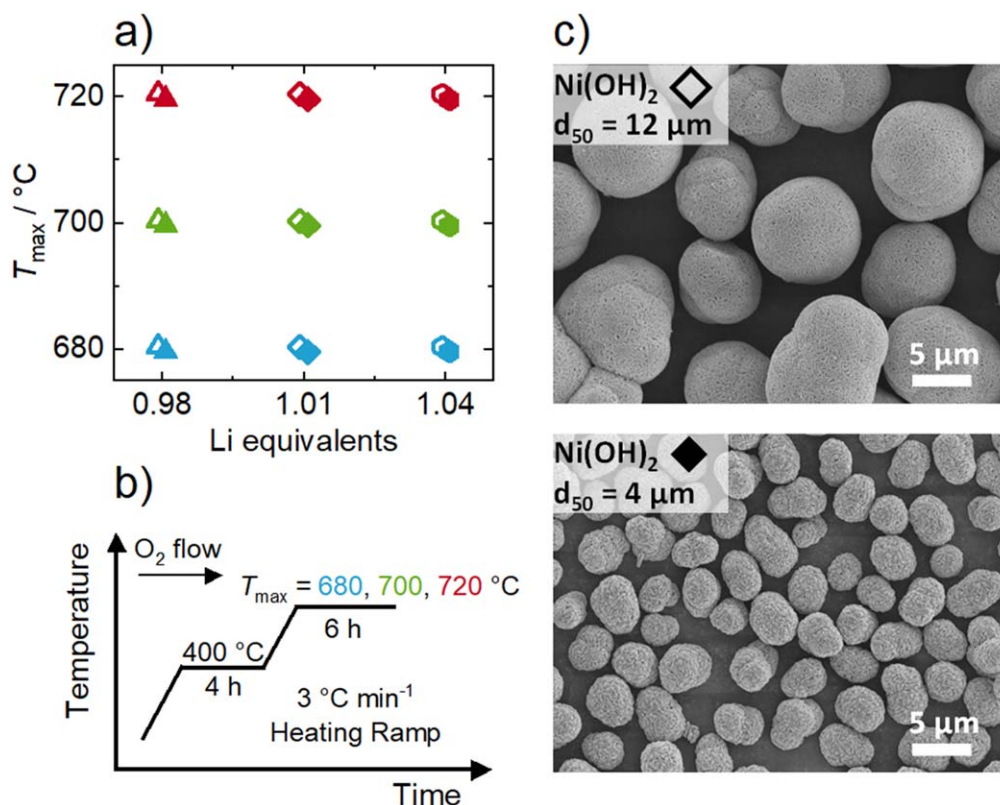


Figure 1. Overview of the samples prepared for this study. (a) Calcination conditions employed, with color referring to three different maximum calcination temperatures T_{max} (680 °C: blue, 700 °C: green, 720 °C: red) and symbols indicating three different Li equivalents per mol of Ni (0.98: triangles, 1.01: diamonds, 1.04: hexagons). (b) Temperature profile used for calcination. (c) Top view SEM images of the two chosen $\text{Ni}(\text{OH})_2$ precursors (precursor with d_{50} of $\sim 12 \mu\text{m}$ marked by empty symbols and precursor with d_{50} of $\sim 4 \mu\text{m}$ marked by filled symbols in (a), respectively). In summary, 18 different samples were prepared.

The LNO samples were filled in borosilicate capillaries of 0.7 mm diameter, sealed by flame, and mounted on a spinning sample holder. Data were collected in Debye–Scherrer geometry for 27 different positions of the detector, and a long data acquisition time of 30 s was chosen for each position in order to obtain high intensity patterns. Rietveld refinement was done using the Fullprof software package.³⁸ For each sample a new background for the measured diffraction pattern was determined with the WinPLOTR software³⁹ and corrected by visual inspection. The refinements were based on a hexagonal α -NaFeO₂ structure with the $R\text{--}3m$ space group.⁴⁰ The instrumental broadening was determined by measuring a NAC (Na₂Ca₃Al₂F₁₄) standard in the same sample configuration. The model used for the fitting is based on Thompson–Cox–Hastings pseudo-Voigt convoluted with axial divergence asymmetry functions. Using the instrumental resolution function, the sample contribution to the peak broadening was determined: with the angular dependence of the peak broadening related to a finite crystallite size described by the Scherrer equation, a volume-averaged value of the crystallite size was obtained.⁴¹ Refinement of the parameters of the structural model was done for consecutive iteration cycles until convergence was reached and the quality of the fit was checked by inspection of R_{wp} (weighted profile factor with all non-excluded points) and R_{Bragg} (Bragg R-factor) as well as χ^2 (reduced chi-square). For all samples, in the final iteration 12 parameters were refined: scale factor, zero shift, a and c unit cell parameters, U , X , Y as parameters of the Gaussian (U) and Lorentzian (X , Y) contribution to the pseudo-Voigt function, fractional atomic coordinate of oxygen z_{ox} , occupancy of Ni on Li site (assuming site remains fully occupied), B_{iso} (isotropic displacement parameter) of O, Ni and of Li. According to the recent report of Yin et al., Li and O were treated using the ionic form factors while the atomic form factor was applied for Ni.⁴² Note that fully atomic and fully ionic form factors were also tested; these resulted in acceptable fits but with slightly larger R_{Bragg} values and too low $B_{\text{iso}}(\text{Li}) \approx 0.3 \text{ \AA}^2$. Yet, all trends reported in this paper would be preserved by a different choice, with an offset of Ni on the Li site of only $z \approx 0.003$. For the two samples of this study (720 °C and 1.04 li equiv.) having the largest crystallite size and therefore smallest peak broadening, the asymmetric shape of the Bragg peaks at low θ was accounted for by two additional parameters refined at a LeBail fit stage, but then constrained later during the Rietveld fit. For all refinements, final values of $R_{\text{wp}} < 11$ and $R_{\text{Bragg}} < 3$ were obtained. Error bars are reported as 3σ , where σ is the error obtained from the Fullprof software.

Magnetization measurements.—The temperature and field dependent magnetization of the pristine powders was measured by a Superconducting Quantum Interference Device (SQUID, MPMS 5XL, Quantum Design Inc.). For each measurement ~ 40 mg of the respective powder was filled into a gelatine capsule, which was then centrally fixed in a plastic straw. The straw was mounted onto the sampling rod of the SQUID. For the field dependent magnetization, the external magnetic field was scanned between -50 and 50 kOe (-5 to 5 T). The measurement was repeated at 300 and 2 K. For the determination of the Weiss constant, a field warming curve of the magnetic susceptibility at an external magnetic field of 10 kOe between 2 and 300 K was recorded. The diamagnetic contribution of the capsule was subtracted from the signal. To account for the diamagnetic contribution of the Li and O ions, the susceptibility was corrected by the use of Pascal’s constants.⁴³

Electrochemical characterization.—Electrodes for electrochemical characterization were prepared by mixing the CAM powders with conductive carbon (C65, Imerys Graphite & Carbon) and PVDF binder (Solef 5130, Solvay GmbH) in a 94:3:3 mass ratio. For this, a 7.5 wt% binder solution in N-methyl-2-pyrrolidone (NMP, BASF SE) was mixed with additional NMP and the conductive carbon, and mixed for at least 24 min at 2000 rpm in a planetary mixer (ARE 250, Thinky Corporation). The CAM powders were

added to the obtained slurry and were mixed for additional 10 min. The solid content of the final slurries was 61 wt%. The slurries were cast onto an Al-foil (thickness 20 μm , Nippon Light Metal Co., Ltd.) using a box-type coater (wet-film thickness 100 μm , width 6 cm, Erichsen GmbH & Co. KG) and an automated coating table (5 mm s⁻¹, Coatmaster 510, Erichsen GmbH & Co. KG). The coated tapes were placed in a vacuum oven (VDL 23, Binder GmbH) and heated to 120 °C under vacuum for drying overnight. The dried cathode tapes were compressed using a calender (CA5, Sumet Systems GmbH) at a set line-force of 30 N mm⁻¹ and a roller speed of 0.5 m min⁻¹. Circular electrodes with a diameter of 14 mm were punched out using a high-precision handheld punch (Nogamigiken Co., Ltd). After weighing, the electrodes were transferred to an Ar filled glovebox for cell assembly. An average loading of (8.0 ± 0.5) mg cm⁻² and an electrode density of (3.0 ± 0.2) g cm⁻³ were obtained. Coin half-cells were built using a 2032 coin cell geometry. The cell stack consisted of the cathode, a glass fiber separator (ϕ 17 mm, 300 μm thickness, GF/D, VWR International, LLC.) soaked with 95 μl electrolyte (LP57, BASF SE) and a pre-punched Li anode (ϕ 15.8 mm, thickness 0.58 mm, purity 99.9%, Shandong Gelon LIB Co., Ltd). After assembly the cells were crimped and closed in an automated crimper (Hohsen Corp.). The cells were then transferred to a climate chamber (Binder GmbH) and connected to a battery cycler (Series4000, MACCOR, Inc.). All tests were performed at 25 °C and the C rates were defined according to 1 C = 200 mA g⁻¹.

Results and Discussion

Synchrotron PXRD measurements and refinement.—The layered compound LiNiO₂ is known to crystallize in a rhombohedral unit cell, isostructural with α -NaFeO₂ with the space group $R\text{--}3m$.^{30,44,45} The layered character of this structure is induced by the different ionic radii of $r(\text{Li}^+) = 76$ pm, $r(\text{Ni}^{2+}) = 69$ pm and $r(\text{Ni}^{3+}_{\text{LS}}) = 56$ pm (LS = low spin).⁴⁶ The oxygen anions on the 6c sites form a cubic close packed lattice and the octahedral interstices are occupied by the Ni and Li cations in the 3a (0, 0, 0) and 3b (0, 0, 0.5) sites, respectively. In this work, only small deviations from perfect stoichiometry in the form of $\text{Li}_{1-z}\text{Ni}_{1+z}\text{O}_2$ were assumed for the Rietveld refinement, which will be substantiated in the following chapter.

Exemplary results of three selected samples from this study with clear variation of calcination conditions are shown in Fig. 2. PXRD patterns of the samples prepared with the 12 μm Ni(OH)₂ (blue: 680 °C, 0.98 li equiv.; green: 700 °C, 1.01 li equiv.; red: 720 °C, 1.04 li equiv.) are depicted in Fig. 2a, demonstrating that LNO with good crystallinity and characteristic reflections is obtained for all employed calcination conditions. The low background and high signal-to-noise ratio indicate the high data quality of the synchrotron setup, which was also observed in other studies on LNO.^{47,48} The magnified views of the 003 peak and of the 108 and 110 peaks in Figs. 2b and 2d, respectively, illustrate the distinct impact of the calcination conditions on crystal structure and morphology. A shift of the peak position to higher scattering angles concomitant with a decrease in full-width-at-half-maximum (FWHM) with increasing maximum calcination temperature T_{max} and Li equivalents is observed. The different angular peak positions are related by Bragg’s law to different lattice parameters for the investigated samples, whereas changes of the peak FWHM are connected to different average crystallite sizes. The observations made for increasing T_{max} and Li equivalents are in line with a decrease in unit cell volume and an increase in average crystallite size. Figure 2c shows a selected angular range, where peaks from Li-containing impurities arise, which can be assigned to LiOH, Li₂CO₃ and Li₂SO₄. LiOH and Li₂CO₃ are present as products of unreacted Li₂O with moisture and CO₂ from ambient air after calcination,^{49,50} despite fast transfer to a dry room. In the literature, these impurities were shown to be located on the surface of the secondary particles.^{51,52} The formation of Li₂SO₄ is plausible regarding the residual sulfur content of the precursor after precipitation starting

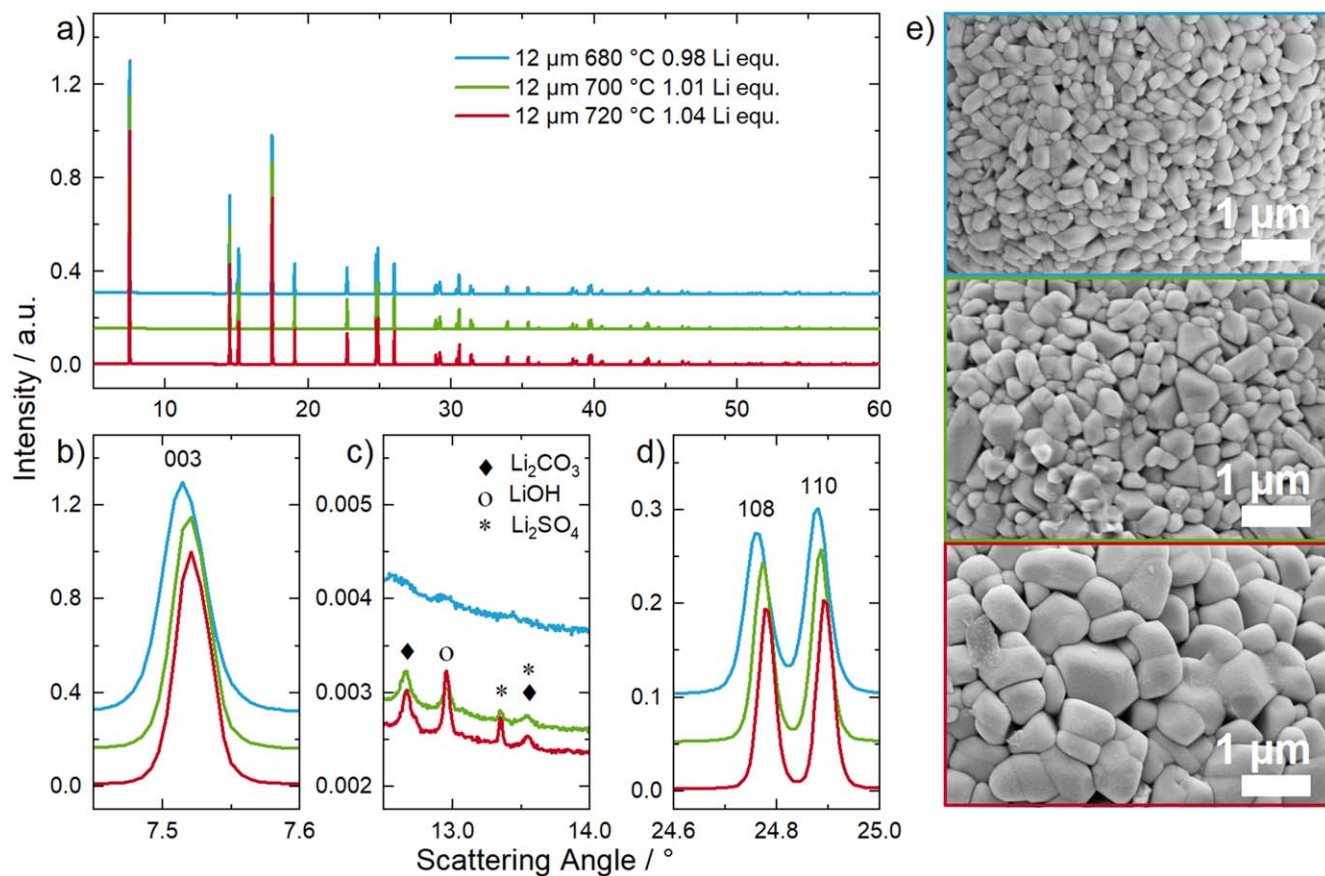
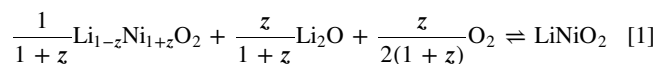


Figure 2. Synchrotron X-ray diffraction patterns and top view SEM images of three exemplary samples prepared from the 12 μm $\text{Ni}(\text{OH})_2$ precursor, for which 0.98 Li equivalents and 680 $^\circ\text{C}$ (blue), 1.01 Li equivalents and 700 $^\circ\text{C}$ (green) and 1.04 Li equivalents and 720 $^\circ\text{C}$ (red) were used as calcination conditions. (a) Full PXRD pattern in the range of $2\theta = 5^\circ\text{--}60^\circ$. (b) Zoom-in of the 003 Bragg peak. (c) Selected peaks assigned to the Li impurities Li_2CO_3 (diamond), LiOH (circle) and Li_2SO_4 (asterisks). (d) Zoom-in of the 108 and 110 Bragg peaks. The data was collected at the BL04-MSPD beamline of the ALBA synchrotron at a set wavelength of $\lambda = 0.62 \text{ \AA}$. (e) Top view SEM images of the three samples in 20 k magnification.

from NiSO_4 feeds, as found for other Ni-rich compositions as well.⁵³ Nevertheless, the contribution of these impurities to the overall PXRD patterns is very small as a large magnification (x200) is required to make them visible. Therefore, the impurities are assumed to not have a detrimental impact on the subsequent refinement of the structural model. To give an overview of the samples' morphology, top view SEM images in 20 k magnification are depicted in Fig. 2e. All CAM samples show distinct primary particles that form a secondary particle agglomerate, which resembles the morphology of the $\text{Ni}(\text{OH})_2$ precursor. Increasing both the number of Li equivalents and T_{max} leads to a clear increase of primary particle size, which will be studied in more detail in a forthcoming report.

To quantify the aforementioned observations, Rietveld refinement of the parameters of the structural model against the PXRD data was performed. The main results of the refinement are summarized in Fig. 3 and all results including error bars can be found in Table I. In Figs. 3a and 3b, the Ni occupancy on the Li site is depicted as a function of T_{max} and the Li equivalents, respectively. Thermal decomposition is an often discussed topic for the synthesis of LNO, as it already occurs at temperatures close to the calcination temperature required to form the stoichiometric compound.^{47,54} In this case, the layered LNO decomposes towards the parent rock salt-type NiO phase (i.e. z increases in $\text{Li}_{1-z}\text{Ni}_{1+z}\text{O}_2$), releasing O_2 and Li_2O , following the backward reaction shown in Eq. 1. The formed Li_2O is hypothesized to be oxidized to Li_2O_2 , which is assumed to be very volatile.^{54,55} However, this topic is still under debate and there is evidence in the literature that the proposed mechanism is not very likely to happen.⁵⁶ Although a slight increase in off-stoichiometry at a higher T_{max} is observed in Fig. 3a, the differences between

samples with the same number of Li equivalents are very small and could presumably not be resolved with a conventional laboratory X-ray setup in contrast to the data acquired at the synchrotron. Therefore, the PXRD analysis shown in Fig. 3a suggests that there is no evidence for a significant impact of thermal decomposition or Li loss into the vapor phase at these calcination temperatures. However, with increasing Li equivalents, a clear decrease in Ni excess in the Li site can be seen in Fig. 3b, indicating the formation of a more stoichiometric LNO with a higher Li excess in the calcination process. Considering reaction Eq. 1, this observation follows Le Chatelier's principle, because a higher amount of Li excess in the calcination pushes the chemical reaction towards the formation of LiNiO_2 as part of the solid solution with NiO.



The results are in good agreement with literature reports showing that the synthesis of LNO samples close to ideal stoichiometry requires a sufficient amount of Li excess.^{36,57} However, these studies often used large increments of Li excess or such high amounts (starting from 7–10 mol% and up to 300 mol%), that a washing step afterwards is necessary to remove residual Li salts after calcination. In terms of raw material costs, this approach is not economically feasible and a washing step should be avoided, which is why the Li excess in this work was limited to 4 mol%. Finally, it should be mentioned that it is possible to synthesize Li-rich compounds related to Li_2NiO_3 by a simple solid-state method using the same starting materials employed in this study, even though more oxidizing

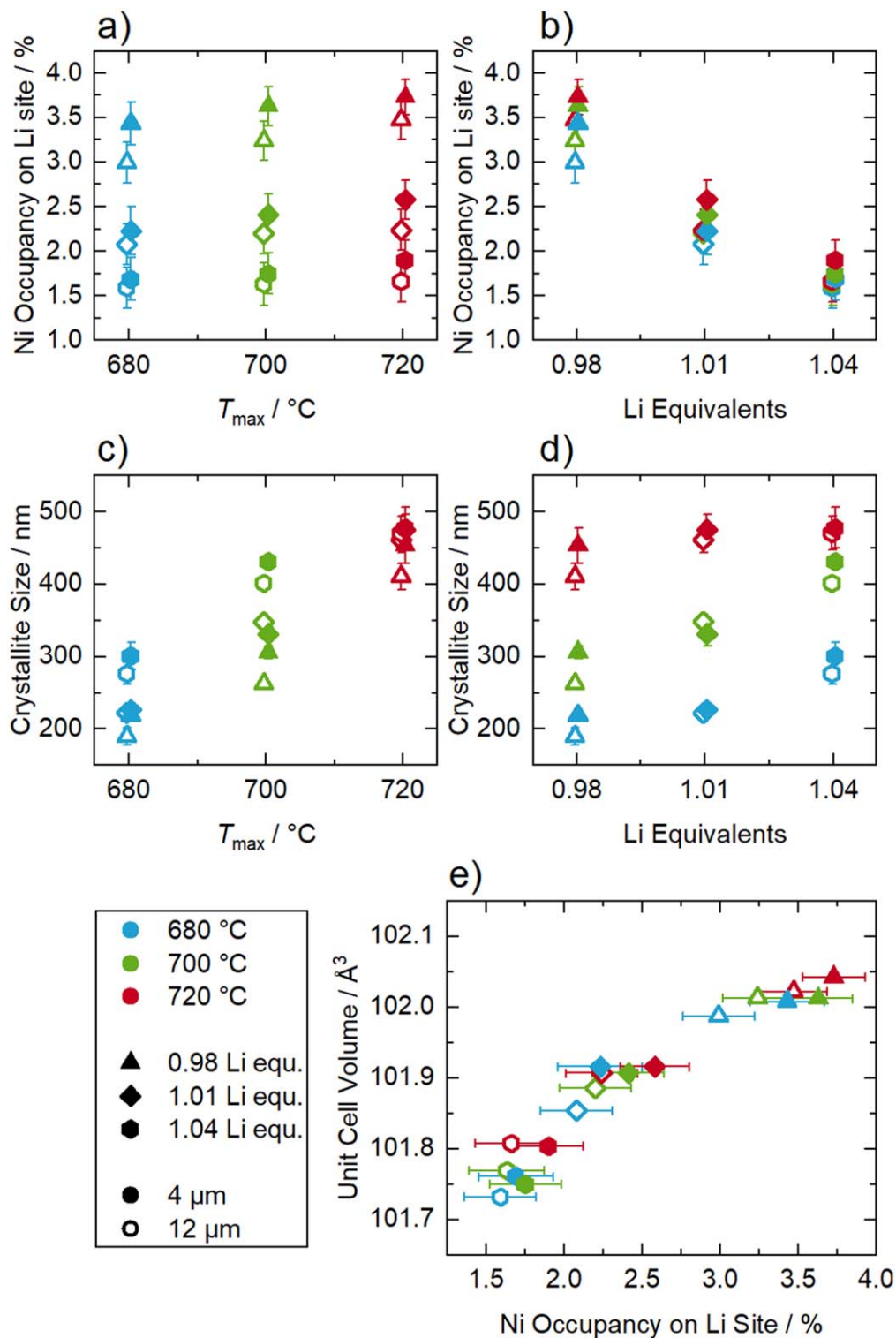


Figure 3. Results of the Rietveld refinement for all LNO samples prepared in this study. All samples were refined assuming Ni excess in the Li layer (sum formula of $\text{Li}_{1-z}\text{Ni}_{1+z}\text{O}_2$). (a) Ni occupancy on the Li site vs the maximum calcination temperature T_{max} (680 °C: blue, 700 °C: green, 720 °C: red) and (b) Ni occupancy on the Li site vs the Li equivalents per mol of Ni added to the calcination (0.98: triangles, 1.01: diamonds, 1.04: hexagons). Samples prepared from the 4 μm precursor are depicted as filled, samples prepared from the 12 μm precursor are shown as empty symbols. (c) and (d) depict the refined crystallite size vs T_{max} and Li equivalents, respectively. For better readability, 4 μm and 12 μm samples are slightly offset in x-direction. (e) Correlation between the Ni occupancy on the Li site and the refined unit cell volume.

conditions are needed in this case to raise the oxidation state of Ni to values larger than +3 (lower calcination temperature and higher Li excess).⁴⁸ Thus, the occurrence of overlithiation can be excluded for the materials prepared in this work.

Figures 3c and 3d depict the average crystallite size from Rietveld refinement as a function of maximum calcination temperature and the Li equivalents. Here, the refined crystallite size shows a clear dependence on T_{max} (from 680 °C to 720 °C) leading to an

Table I. Results of the Rietveld refinement for all samples calcined in this study: Ni occupancy on the Li sites, unit cell volume (UCV), average crystallite size, fractional atomic coordinate of oxygen z_{ox} , B_{iso} of O, Ni and Li. R_{Bragg} , R_{wp} and χ^2 are depicted to underline the goodness of the refinement.

Sample	Ni occ./%	UCV/ \AA^3	Size/nm	z_{ox}	B_{iso} O	B_{iso} Ni	B_{iso} Li	R_{Bragg}	R_{wp}	χ^2
12 μm										
0.98 680 °C	3.0(2)	101.987	189(12)	0.2585(2)	0.94(4)	0.358(8)	0.7(1)	2.33	9.51	33.8
0.98 700 °C	3.2(2)	102.013	263(6)	0.2586(2)	0.92(3)	0.346(8)	0.8(1)	2.03	8.96	33.2
0.98 720 °C	3.5(2)	102.022	410(19)	0.2585(2)	0.97(3)	0.395(8)	0.9(1)	1.72	8.82	40.0
1.01 680 °C	2.1(2)	101.854	222(11)	0.2586(2)	0.92(4)	0.354(8)	0.8(1)	2.21	9.54	35.6
1.01 700 °C	2.2(2)	101.886	348(10)	0.2586(2)	0.99(3)	0.426(8)	0.9(1)	1.85	9.14	44.4
1.01 720 °C	2.2(2)	101.907	461(16)	0.2586(2)	0.97(3)	0.407(8)	0.9(1)	1.71	9.40	47.4
1.04 680 °C	1.6(2)	101.732	277(15)	0.2586(2)	0.92(3)	0.384(8)	0.9(2)	1.84	9.41	48.2
1.04 700 °C	1.6(2)	101.769	401(4)	0.2586(2)	0.93(3)	0.377(8)	0.9(2)	1.62	9.52	47.5
1.04 720 °C	1.7(2)	101.808	470(23)	0.2587(2)	0.93(3)	0.386(8)	0.9(1)	1.74	9.26	44.2
4 μm										
0.98 680 °C	3.4(2)	102.008	219(7)	0.2583(2)	0.97(4)	0.383(9)	0.9(1)	2.07	9.85	61.9
0.98 700 °C	3.6(2)	102.012	306(9)	0.2583(2)	0.96(3)	0.386(8)	0.9(1)	2.11	9.14	63.1
0.98 720 °C	3.7(2)	102.042	453(25)	0.2583(1)	1.02(3)	0.442(7)	0.9(1)	1.86	7.98	46.2
1.01 680 °C	2.2(3)	101.916	227(9)	0.2585(2)	1.02(4)	0.428(10)	0.9(2)	1.87	10.8	81.0
1.01 700 °C	2.4(2)	101.907	331(17)	0.2585(2)	0.94(4)	0.369(8)	0.9(1)	1.78	9.39	57.3
1.01 720 °C	2.6(2)	101.916	475(21)	0.2584(2)	0.97(3)	0.402(8)	0.9(1)	1.70	8.86	57.8
1.04 680 °C	1.7(2)	101.761	301(19)	0.2585(2)	0.96(4)	0.414(9)	1.0(2)	1.74	9.66	69.5
1.04 700 °C	1.8(2)	101.750	432(9)	0.2586(2)	0.95(3)	0.409(8)	1.0(2)	1.53	8.99	64.1
1.04 720 °C	1.9(2)	101.804	478(28)	0.2586(2)	0.99(3)	0.443(8)	1.0(1)	1.51	8.64	53.7

increase of average crystallite size by a factor of ~ 2 (200–300 nm to 400–600 nm) for the two utilized precursors. During the high temperature hold, larger crystallites grow at the expense of smaller ones to reduce the free surface energy of the system, a process which is promoted by higher calcination temperatures.⁵⁸ Few reports exist on the dependence of the crystallite size on the calcination temperature for polycrystalline LNO or NCM compounds.^{59,60} However, these reports claim average crystallite sizes below 100 nm for LNO and Ni-rich NCM calcined under comparable conditions, which could be ascribed to the very different starting precursors or to limitations of the PXRD setups used in these studies.

For a given T_{max} , an increase in average crystallite size with increasing Li equivalents is also observed (Fig. 3d), although the impact is less pronounced compared to the one of the calcination temperature (Fig. 3c). Parts of the molten Li source can act as a flux before it completely reacts with NiO at elevated temperatures, which can promote the growth of already present crystallites similar to other flux methods.⁶¹ However, in the chosen range of calcination parameters, the calcination temperature is always the more decisive factor for the crystallite size compared to the number of Li equivalents. Following the current trend in research moving from polycrystalline materials to single crystal morphology, the finding that the crystallite size increases with T_{max} and Li excess is in good agreement with typical approaches to calcine materials with monolithic structures.^{19,62} In comparison to these methods, the calcination conditions from this study are however rather moderate, with the final CAM still maintaining the polycrystalline secondary particle structure of the precursors. It must be mentioned that the crystallite size should not be confused with the primary particle size that can be seen in the SEM images in Fig. 2e. The term “crystallite size” here refers to the size of the coherently scattering domains, and each primary particle can consist of one or more of these crystallites.⁶³ Moreover, the Rietveld refinement provides only values of the crystallite size averaged over the whole powder sample. There are methods to extract the particle size distribution from Rietveld refinement, although they depend on the assumption of a certain distribution function.⁶⁴ Quantitative information on the primary particle size distribution can be obtained with SEM image segmentation and the respective results for this calcination study will be presented in a forthcoming report.

Figure 3e depicts the unit cell volume as a function of the Ni occupancy on the Li site. As shown in the literature, the unit cell volume shows a linear increase with increasing Ni excess (Vegard’s law along the NiO–LiNiO₂ solid solution).^{36,65} So far it was difficult to show this relation for Li_{1–z}Ni_{1+z}O₂ with small values of z due to the scattering of data points for materials made by different groups and measured with different instruments. However, here this relationship can be confirmed even for $0.016 \leq z \leq 0.037$, refining the parameters of the structural model, which is based on the observed high-quality synchrotron PXRD data. Extrapolation to $z = 0$ leads to a unit cell volume of 101.56 \AA^3 , which is in line with other reported extrapolations for LNO with ideal stoichiometry.³⁰

In principle, a second scenario in competition to the off-stoichiometry would be possible with Li/Ni antisite defects, i.e. a site exchange of small amounts of Li and Ni (often called “Li/Ni disorder” or “Li/Ni exchange”).²⁸ This kind of defect is often discussed for NCM compositions, and the formation energy of such defects was shown to be dependent on the total fraction of Ni²⁺ ions.⁶⁶ Thus, it is frequently observed for materials which contain Mn⁴⁺ as this requires an equal amount of Ni²⁺ for charge compensation. For LNO, however, which contains virtually no Ni²⁺, the energy required to form antisite defects is very large (> 340 meV defect⁻¹) and off-stoichiometry is considered the dominating source of defects. Due to the small Li X-ray cross-section, directly proving the defects’ nature is difficult. However, neutron diffraction studies showed that for small Li deficiency (namely $z = 0.02$ or 0.07), no Li/Ni disorder occurred and mixing was only determined for a large deficiency of $z = 0.25$.⁶⁷ In other studies, researchers also suggested oxygen vacancies in LNO in the context of synthesis under pressurized oxygen atmosphere and claimed the representation Li_{1–z}Ni_{1+z}O_{2–y} to account for these oxygen vacancies.⁶⁸ The formation energy of oxygen vacancies was examined by DFT calculations, and vacancy formation could become energetically favorable at high temperatures during calcination, but this is more likely to happen at the surface and especially in the delithiated state.^{69,70} However, as oxygen vacancies were never confirmed for LNO using neutron diffraction measurements, they were not included in the structural model used in this study. The general goodness of the Rietveld refinement for all investigated samples (see Table I) and the observed continuation of the linear

relationship between unit cell volume and Ni excess in the tested parameter space strengthen the assumption of off-stoichiometry and of absence of intrinsic antisite defects and overlithiation.

Magnetic properties of LiNiO₂.—The procedure of determining the Ni occupancy on the Li site by Rietveld refinement is model-dependent and thus a cross-validation with other methods is highly desirable. An often overlooked property of the materials that correlates with its crystallographic properties is the magnetic behavior. Even before its application as cathode active material, the magnetic properties of the Li_{1-z}Ni_{1+z}O₂ system have been investigated by Goodenough et al.⁴⁵ The electronic configuration of Ni³⁺ in an octahedral coordination environment and the view along the *c*-axis on top of the Ni slab of the stoichiometric LNO crystal structure are depicted in Fig. 4a. With the orbital energetic levels being split into two e_g and three t_{2g} states and the Ni³⁺ electron configuration being 3d⁷, a doublet electronic configuration (*S* = 1/2) with a single unpaired electron is expected, which can interact with an external magnetic field. Even if LNO is reported as a “non-cooperative” or “dynamic” Jahn-Teller system, the material remains a *S* = 1/2 system.⁷¹ Because the Ni ions sit on a triangular lattice for perfectly crystallized LiNiO₂, no long-range magnetic ordering is expected to form due to quantum mechanical frustration of the

electron spins,⁷² which motivated the investigation of near-stoichiometric LNO compounds.^{73–75} Given the interest in LNO as CAM, several authors investigated the magnetic properties of Li_{1-z}Ni_{1+z}O₂ in narrow ranges of *z*.^{34,36,76,77} All authors observed a transition from paramagnetic behavior at high temperature towards a state of magnetic long-range ordering below a certain temperature, coming with a rapid increase of the magnetic susceptibility. Due to the fact that magnetic ordering is correlated to the presence of excess Ni²⁺ in the Li layers, coupling different Ni layers, it was found that this transition shifted towards higher temperatures with increasing values of *z*. This makes the measurement of temperature-dependent magnetization a powerful tool to investigate site occupation and lattice defects in LNO.

Figure 4b shows the field dependent magnetization curves of one exemplary LNO sample measured at 2 K and 300 K. The inset shows a magnification of the magnetization in a range of –2 to 2 kOe. While paramagnetic behavior is observed at 300 K, a hysteretic feature is observed at 2 K, indicative of magnetic ordering. Although the exact mechanism of this magnetic ordering is still under debate in the literature, as mentioned above there is consensus that it is related to the excess Ni²⁺ on the Li site. Materials showing a transition between the paramagnetic regime and magnetic ordering can be described by the Curie-Weiss law shown in Eq. 2.

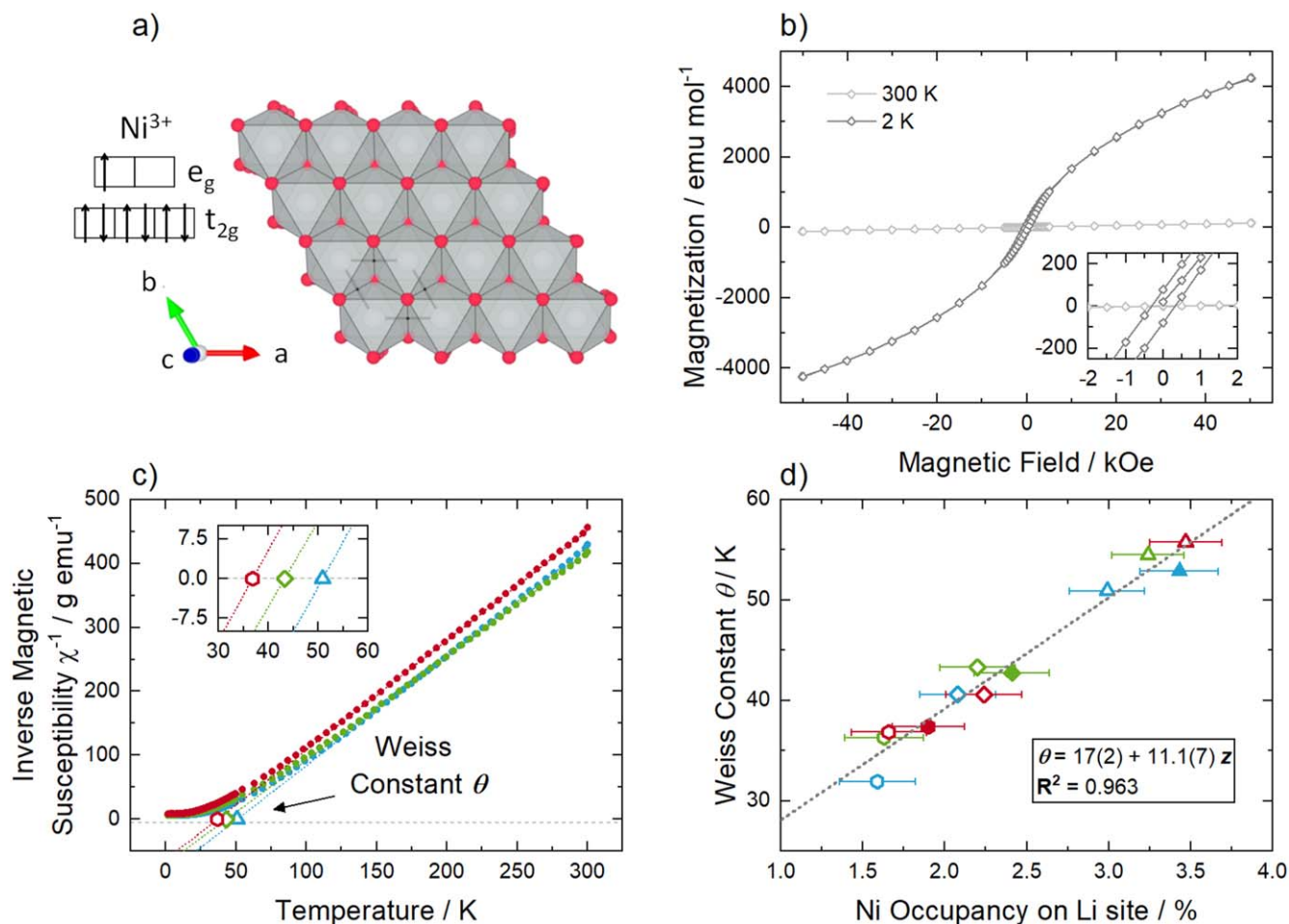


Figure 4. Magnetization results obtained from SQUID-measurements for selected samples. (a) Electronic configuration of Ni³⁺ in octahedral coordination and view along the *c*-axis on top of the Ni slab. (b) Magnetization curve of the LNO sample prepared from the 12 μm precursor with 1.01 Li equivalents per mol of Ni at a maximum calcination temperature of 700 °C. Two sets of measurements between –50 and 50 kOe were performed at 2 K (dark grey) and 300 K (light grey), respectively. The inset shows a magnified view of the magnetization at low external field values, highlighting the hysteretic behavior at the low measurement temperature. (c) Dependence of the inverse magnetic susceptibility on the measurement temperature at an external field of 10 kOe for three LNO samples prepared from the 12 μm precursor (blue: 680 °C Li equiv., green: 700 °C 1.01 Li equiv., red: 720 °C 1.04 Li equiv.). The Weiss constant θ was determined by performing a linear regression between 150 and 300 K and interpolating on the x-axis. (d) Correlation of the determined Weiss constant θ with the Ni occupancy on the Li site. The grey dotted line represents a linear regression through all data points.

Table II. Results from magnetization measurements for all samples calcined from the 12 μm Ni(OH)₂ precursor and for three exemplary samples calcined from the 4 μm Ni(OH)₂ precursor: weiss constant θ and Curie constant C .

Sample	θ/K	$C/\text{m}^3 \text{K mol}^{-1}$
	12 μm	
0.98 680 °C	50.90	0.59
0.98 700 °C	54.50	0.59
0.98 720 °C	55.73	0.58
1.01 680 °C	40.59	0.56
1.01 700 °C	43.29	0.62
1.01 720 °C	40.60	0.62
1.04 680 °C	29.93	0.62
1.04 700 °C	36.30	0.59
1.04 720 °C	36.85	0.58
	4 μm	
0.98 680 °C	53.00	0.58
1.01 700 °C	42.91	0.59
1.04 720 °C	37.60	0.57

$$\chi = \frac{C}{T - \theta} \quad [2]$$

Here χ denotes the magnetic susceptibility, C is the Curie constant, T is the measurement temperature and θ is the Weiss constant, which is the transition temperature between paramagnetic and hysteretic magnetic behavior. The Weiss constant can be determined by a linear regression of the inverse magnetic susceptibility in the paramagnetic regime (150–300 K) and extrapolating to the temperature axis. The inverse magnetic susceptibility χ^{-1} as a function of temperature and the regression are depicted in Fig. 4c for three exemplary LNO samples prepared from the 12 μm Ni(OH)₂ (blue: 680 °C, 0.98 li equiv.; green: 700 °C, 1.01 li equiv.; red: 720 °C, 1.04 li equiv., analogous to Fig. 2). The results for θ for all materials from this study are well correlated to the Ni occupancy on the Li site determined by Rietveld refinement, as shown in Fig. 4d (all measured values of θ are depicted in Table II). The linear dependency indeed indicates a clear correlation between Ni excess and magnetic behavior of the LNO samples and is in good agreement with the results of the above-cited groups, even for very small values of z .^{76,77} Although this finding corroborates the trend of Ni excess in its qualitative nature, it alone is not a confirmation of the assumed model and the absence of antisite defects. Another information that can be derived from the fit of χ^{-1} is the Curie constant C . For a given material with n unpaired electrons that behaves like a paramagnet, the expected Curie constant in the spin-only case (no spin-orbit coupling) follows Eq. 3.

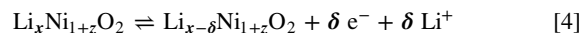
$$\chi T = C = \frac{1}{8}(n(n+2)) \quad [3]$$

Hence, a Curie constant of 0.375 (unit: $\text{m}^3 \text{K mol}^{-1}$) is expected for stoichiometric LiNiO₂. In the applied model for Rietveld refinement, an increase in the off-stoichiometry z comes with the generation of $2z$ Ni²⁺ ions and thus additional unpaired electrons. An increase of z by 0.01 in theory would equal an increase of C by 0.05. However, the determined Curie constants for the different samples, as shown in Table II, range from 0.56 to 0.62 (with a large scatter, but the appearance of decreasing C with increasing z) and clearly deviate from the single unpaired electron picture. Nevertheless, the results are in line with other reports.^{34,77} Possible explanations for this deviation might lie in the enhancement of Landé g factor caused by a local Jahn-Teller effect, as for NaNiO₂, or orbital contributions.^{78,79}

These results confirm that magnetization measurements using a SQUID are a valuable tool for the characterization of battery active materials, even for samples with only minor differences in crystal structure. With magnetization measurements becoming feasible in situ inside an assembled cell, where changes of magnetic properties during electrochemical (de-)lithiation can be monitored, these investigations are expected to attract more interest of CAM researchers in the future.^{80,81}

Impact of structural chemistry on the voltage profile.—After determining the crystal structure, crystallite size and magnetic properties of the calcined samples, their electrochemical behavior was investigated by employing galvanostatic cycling and analysis of the differential capacity (dQ/dV) plots.

The measured voltage of a given electrochemical reaction is the sum of the thermodynamic voltage of the reaction and the overpotentials corresponding to the cell impedance. For a LNO half-cell, the occurring reaction during oxidation is shown in Eq. 4.



In this case x is in the range between 0 and $1-z$ in case of full delithiation and lithiation, respectively, and δ denotes the number of transferred electrons. The thermodynamic (open cell) voltage E is intrinsically linked to the Gibbs free energy $\Delta_r G$ of the underlying

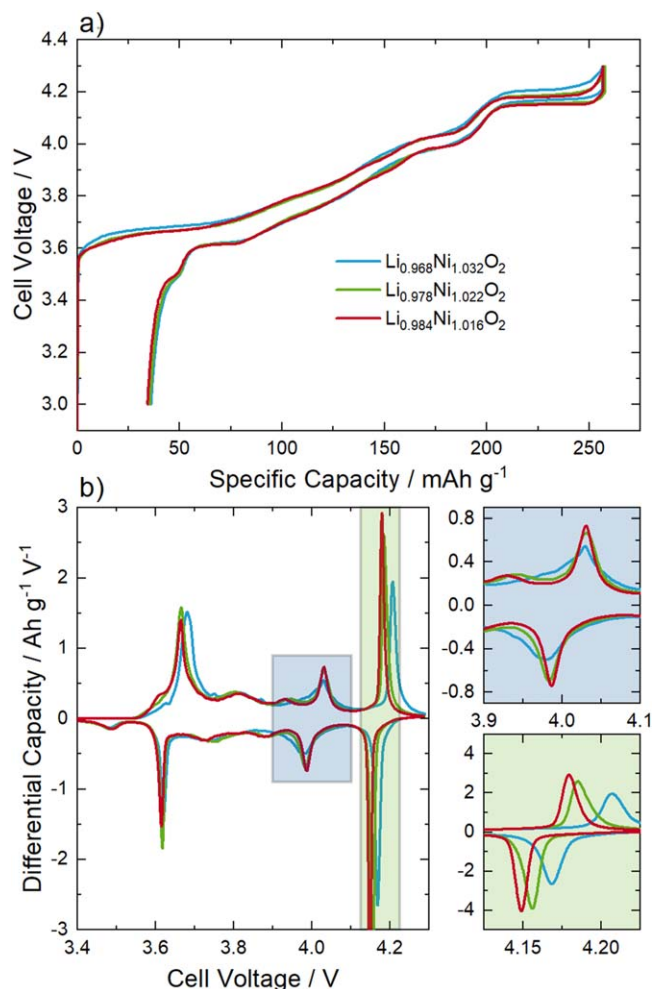


Figure 5. Voltage profile analysis of LNO samples with distinctly different values of z in $\text{Li}_{1-z}\text{Ni}_{1+z}\text{O}_2$. The samples correspond to the materials prepared from the 12 μm precursor at the same maximum calcination temperature of 700 °C and varying number of Li equivalents per mol of Ni. (a) Cell voltage vs specific capacity of the 1st cycle for $z = 0.032(2)$ (blue), $z = 0.022(2)$ (green) and $z = 0.016(2)$ (red) with the stoichiometry determined by Rietveld refinement. (b) Differential capacity vs cell voltage. Two magnifications of the data in the range of 3.9–4.1 V and 4.125–4.225 V are shown. The cells were cycled at C/10.

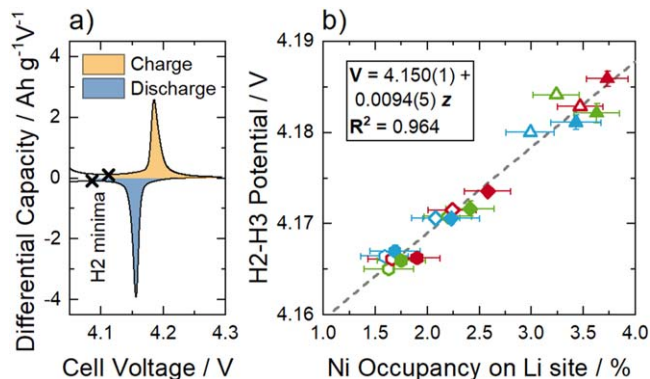


Figure 6. Correlation of the mean potential of the H2–H3 phase transition with the Ni occupancy on the Li site. (a) The potential of the phase transition was determined by taking the mean potential between the minimum of the dQ/dV curve before the H2–H3 peak onset and 4.3 V for charge and discharge. (b) Mean potential of the H2–H3 phase transition as a function of the Ni occupancy on the Li site determined by Rietveld refinement for all samples of this study. The y-error bars depict the standard deviation over at least three cells (only small deviations are obtained). The grey dashed line depicts a linear regression through all data points.

reaction and is depicted for the case of oxidation of LNO during charge in Eq. 5 as:

$$E = -\frac{\Delta_r G}{nF} = -\frac{G_{\text{Li}_x\text{Ni}_{1+z}\text{O}_2} - \delta G_{\text{Li}} - G_{\text{Li}_{x-\delta}\text{Ni}_{1+z}\text{O}_2}}{\delta F} \quad [5]$$

Here, $n = \delta$ is the number of transferred electrons and F is the Faraday constant. With a change in LNO stoichiometry described by the value of z , the underlying reaction changes and might impact the state of charge-dependent thermodynamic voltage, that can easily be probed by a simple electrochemical measurement when a correction for the overpotential is considered. Figure 5a shows the voltage profiles of three exemplary LNO samples from this study prepared from the 12 μm Ni(OH)₂ precursor with distinct values of Ni excess that were determined by Rietveld refinement (blue: $z = 0.032(2)$, green: $z = 0.022(2)$ and red: $z = 0.016(2)$). At first sight, all voltage profiles look very similar, again highlighting the proper crystallization of all samples as indicated by the PXRD results. However, small changes in the voltage profiles can be made visible by calculating the dQ/dV curves, which are shown in Fig. 5b. For LNO, distinct voltage plateaus (peaks in the dQ/dV curve) are observed, which are the result of several phase transitions of the material during (de-)lithiation. These individual phases can be distinguished in ex situ as well as in situ PXRD measurements, as confirmed by the work of several groups.^{31,40,82–88} In the general consensus, there are three phase transitions identified by PXRD during continuous delithiation, separating four single-phase domains occurring in the following order: H1 ($1 > x > 0.75$) to M ($0.63 > x > 0.4$) to H2 ($0.33 > x > 0.25$) to H3 ($0.12 > x > 0$). The phases are named by their symmetry (H: hexagonal, M: monoclinic) and their order of appearance during delithiation. Due to the Gibbs' phase rule, the two-phase regions correspond to voltage plateaus as observed in Fig. 5a, while single-phase regions show relatively steep voltage changes. The single-phase regions are easier to spot in the dQ/dV representation, where they occur as local minima. However, it is important to note that only four phases have ever been observed by PXRD, while seven minima are identified on the dQ/dV curve. They coincide with certain values of x (1, 3/4, 5/8, 1/2, 2/5, 1/4, 1/8). This is well in line with recent first-principles calculations, where all those degrees of lithiation are predicted to form ordered Li arrangements that are energetically favorable.⁸⁸ Yet some of these states are only stable at 0 K, while at higher temperatures they are destabilized by entropic contributions. As a consequence, for example, only one monoclinic region is observed

structurally by PXRD, instead of a sequence of stable phases $x = 5/8, 1/2, 2/5$. Nonetheless, the thermodynamic signature of these phases is visible in the dQ/dV curve, and it is possible that they are still stabilized at the local scale, which would be hard to detect by means of PXRD and electron diffraction would be needed to observe them.⁸⁹

The differential capacity peaks associated with the discussed phase transitions can be found for all samples with different values of z . Nevertheless, with a change of z in $\text{Li}_{1-z}\text{Ni}_{1+z}\text{O}_2$, some differences are observed in two distinct voltage ranges, which are highlighted in the magnified segments of Fig. 5b. In the voltage range between 3.9–4.1 V (marked by the blue shaded area and the blue shaded inset), materials with a small Ni excess show two distinct peaks with a clear local minimum (red and green lines in Fig. 5b). This minimum corresponds to a stable phase that was predicted by first-principles calculations ($\text{Li}_{0.4}\text{NiO}_2$, $x = 2/5$).^{88,90} With an increasing amount of Ni in the Li layer, this minimum vanishes as observed for the sample with $z = 0.032$ (blue line in Fig. 5b). This indicates that the presence of a critical Ni excess is disrupting the arrangement of the Li ions and vacancies, thus making the formation of that phase energetically less favorable. However, the most pronounced change in the voltage profile is observed in the range between 4.125–4.225 V, marked by the green shaded area/inset, i.e. where the H2 to H3 phase transition occurs. Here, for increasing values of z , a shift of the phase transition (peak position in the dQ/dV) to higher potentials is clearly observed. The fact that this happens both during charge and discharge excludes overpotentials to be causing this effect and thus indicates that a change of the thermodynamics related to the phase transition must occur. Besides the peak position changes, also a widening of the peak width is seen in the dQ/dV plots with increasing z , which is often discussed to be related to a suppression of the phase transition, i.e. to the progressive narrowing of the H2–H3 miscibility gap.^{16,91,92}

A clear assignment of the z values to a peak voltage is difficult, which is why we tried to define clear and stringent rules for calculating the mean potential of the phase transition. By assuming that minima in the dQ/dV curve correspond to single-phase regions, the minimum in the dQ/dV curve between 4.0 V and 4.16 V was determined (related to the H2 phase), which is depicted in Fig. 6a. Individually for charge and discharge, the mean potential of the dQ/dV peak between the H2 minimum and the upper cut-off voltage of 4.3 V was calculated. Then, the mean was taken again between the charge and discharge value to cancel out the overpotential and obtain the thermodynamically defined potential. Our correction of the overpotential assumes that it is symmetric for both oxidation and reduction processes. We have observed that indeed this assumption is verified in our case, as the cells were cycled at low currents (20 mA g⁻¹). Asymmetries may be expected only at higher C rates.⁹³ The results for all samples from this study are shown in Fig. 6b as a function of the Ni occupancy on the Li site determined by Rietveld refinement. This comparison shows a clear linear correlation between these values, with an increase of the potential of the phase transition of ~ 9 mV per increase of 1% Ni excess. This observation confirms a correlation between the exact LNO stoichiometry and the hereby determined thermodynamic potentials of the LNO phases.

Equation 5 can be used to understand this behavior and can be rewritten to reflect the H2–H3 phase transition voltage change as a function of z , i.e. ΔE_z , as shown in Eq. 6.

$$\Delta E_z = -\left(\frac{G_{\text{H}2,z} - G_{\text{H}3,z} + (x_{\text{H}2,z} - x_{\text{H}3,z})G_{\text{Li}}}{(x_{\text{H}2,z} - x_{\text{H}3,z})F} - \frac{G_{\text{H}2,\text{LNO}} - G_{\text{H}3,\text{LNO}} + (x_{\text{H}2,\text{LNO}} - x_{\text{H}3,\text{LNO}})G_{\text{Li}}}{(x_{\text{H}2,\text{LNO}} - x_{\text{H}3,\text{LNO}})F} \right) \quad [6]$$

Here, $G_{\text{H}2,z}$ and $G_{\text{H}3,z}$ represent the Gibbs free energy of the H2 and H3 phases of a off-stoichiometric LNO, respectively, while $G_{\text{H}2,\text{LNO}}$

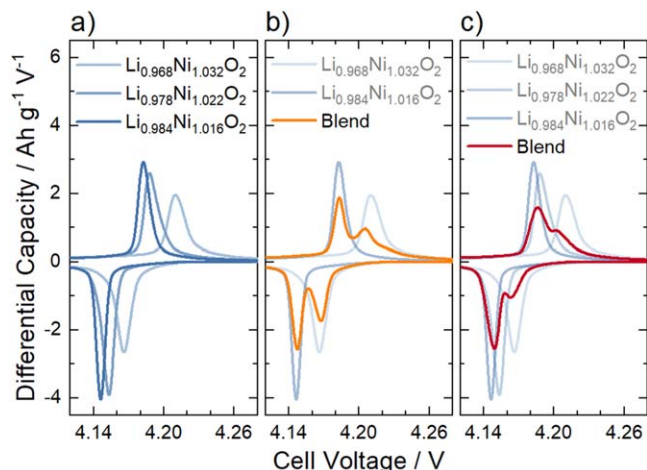


Figure 7. 1st cycle differential capacity of the H2–H3 phase transition of LNO electrodes consisting of different blends of off-stoichiometric LNO samples. (a) Differential capacity of pure materials already discussed in Fig. 5. (b) Differential capacity of a 50/50 blend of two LNOs that differ significantly with regards to their off-stoichiometry. The blended electrode is depicted in orange, with the curves of the pure materials being shown as transparent overlays. (c) 33/33/33 blend of all three materials.

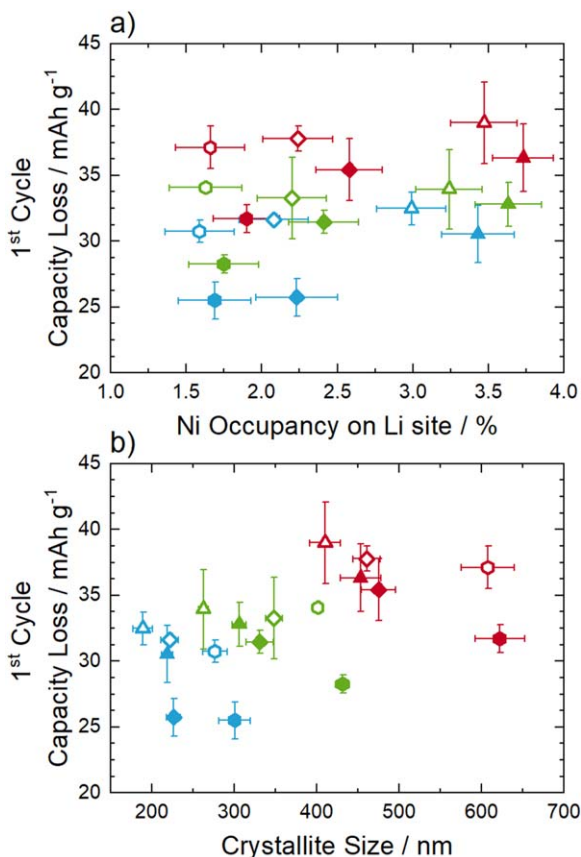


Figure 8. 1st cycle capacity loss vs (a) Ni occupancy on the Li site and (b) crystallite size from Rietveld refinement. In (a) no correlation can be observed. In (b) a weak correlation is present. The cells were cycled at $C/10$ at a temperature of 25 °C.

and $G_{H3,LNO}$ represent the Gibbs free energy of the H2 and H3 phases of a hypothetical perfectly stoichiometric LNO, respectively. The different x values represent the compositions at which the H2 and H3 phases occur. Experimentally, Fig. 5a demonstrated that for small values of z , the compositional span of the H2 to H3 transition

is not significantly narrowed with increasing z ($x_{H2,z} - x_{H3,z} \approx x_{H2,LNO} - x_{H3,LNO} \cong x_{H2} - x_{H3}$). Likewise, the voltage at which the H2 single phase occurs does not appear to be affected for small values of z as the relative minimum in the dQ/dV plot in Fig. 5b does not shift, which means that $G_{H2,z} - G_{H2,LNO} \approx 0$. This ultimately leads to an approximation of ΔE_z depicted in Eq. 7:

$$\Delta E_z = - \left(\frac{G_{H3,LNO} - G_{H3,z}}{(x_{H2} - x_{H3})F} \right) \quad [7]$$

In light of Eq. 7, an increased voltage of the H2–H3 phase transition indicates a larger energetic difference between the Gibbs free energy of the H2 and H3 phases. In other words, as z increases, the H3 phase becomes thermodynamically destabilized compared to the others, and to H2 in particular. We speculate this is due to the H3 phases having a significantly smaller c unit cell parameter and hence Li interlayer thickness, where accommodating a Ni cation can be less favourable.

The hereby reported clear correlation between z and the average H2–H3 transition potential allows to draw conclusions about the stoichiometry of the samples by a rather simple quantitative analysis of the voltage profiles. This can be an extremely valuable tool to complement the stoichiometry obtained by PXRD refinement.

As mentioned above, the dQ/dV plot does not only reveal an increase of the average transition potential with increasing off-stoichiometry, but also a broadening of the H2–H3 peak related to a larger average slope of the voltage curve. A broadening of the peak in the dQ/dV curve is often associated with a narrower miscibility gap, namely the phase transition is progressively evolving towards the formation of a solid solution. This implies that crystallographic stresses are reduced by avoiding the sudden anisotropic volume changes of the H2 to H3 phase transition. This peak shape is known for mid-Ni NCM materials, where the anisotropic volume changes are less pronounced.¹¹ However, here we show that care must be taken in interpreting dQ/dV peak broadening behavior, as the broadening can also be mimicked by the formation of sample inhomogeneities, where severe phase transitions inside the individual particles still occur, but the overlapping H2 to H3 transition peaks merge to yield broad features in the dQ/dV plots. This phenomenon is demonstrated in Fig. 7. In Fig. 7a the dQ/dV curves of three individual LNO samples are shown, which have already been depicted in Fig. 5. In Fig. 7b, the dQ/dV curve of a 50/50 weight ratio mixture of the samples with $z = 0.016(2)$ and $z = 0.032(2)$ is depicted (the individual dQ/dV profiles are again shown in transparent colors). Figure 7c analogously shows the dQ/dV features for the 33/33/33 weight ratio mixture of all three samples (additionally including the sample with $z = 0.022(2)$).

Blending different CAMs leads to a superposition of the voltage profiles according to their relative weight contents.⁹⁴ Only a slight shift of the overpotentials is observed due to an inhomogeneous current load at different SOCs.⁹⁵ Already in the measurement with a blend of three samples, the peak broadening due to different stoichiometries can be observed and the individual peaks cannot be perfectly resolved any more. This indicates that samples with more material inhomogeneities will show only one peak with a large width. In large-scale production, one can easily imagine that due to difficulties of keeping constant calcination parameters (temperature, atmosphere, mixing of individual components) severe powder inhomogeneities can occur.⁹⁶ In this case, the peak width can be used as a measure for the powder inhomogeneity. However, in studies where a suppression of the detrimental phase transition is targeted by modification of the materials (e.g. doping and coating), the possibility of powder inhomogeneities causing the peak broadening is often overlooked. Thus, additional information on the structural properties going beyond the electrochemical testing is always needed to deconvolute the two effects.

Correlation with 1st cycle capacity loss.—Since the early investigations of LNO as cathode active material, researchers have

sought to draw a connection between the Ni excess in the Li layer and the poor 1st cycle reversibility.^{31,32,57} Some authors tried to find empirical correlations between those values, but looked at very large variations of z (0.01–0.12).³⁶ Even for samples in which Ni was substituted for other elements, the decrease of the 1st cycle coulombic efficiency is linked to the increase of excess Ni in the Li layer.⁹⁷ An early explanation for this phenomenon in case of LNO was found in the oxidation of the intralayer Ni²⁺ to Ni³⁺, leading to a local contraction of the crystal lattice and hence poor Li mobility.³²

The large 1st cycle capacity loss is not only an inherent property for LNO, but is also found for most NCMs, making the narrowing of this gap a key target to maximize energy density.²⁴ The origin of the poor reversibility was shown to be of kinetic origin by a multitude of studies and can for example be reduced by the application of a CV step at the end of discharge²⁵ or an increase of cycling temperature.²⁶ Experiments looking at the apparent diffusion coefficients⁹⁸ or Li mobility by NMR experiments⁹⁹ further underline this problem. While a negative effect of excess Ni on the Li mobility is certain, we used our calcined samples to further investigate correlations between small variations of z and the 1st cycle capacity loss.

As the Ni excess has been carefully quantified in this study for a large set of samples and as the observed trends were confirmed by several independent techniques, this alleged correlation can be probed. The 1st cycle capacity loss as a function of the Ni excess determined by PXRD refinement is depicted in Fig. 8a. In contrast to the aforementioned belief, *no correlation* between these quantities is observed. Samples with similar values of z show substantial differences in 1st cycle capacity loss up to 10 mAh g⁻¹. Furthermore, only a slight systematic difference between the CAMs based on the 4 μm and 12 μm precursors is observed, indicating a low impact of secondary particle morphology onto the electrochemical performance. In view of the narrow parameter space of this study and the precise data, another underlying physical parameter must therefore cause the observed differences.

Besides the broadly discussed crystallographic properties and the difference in secondary particle structure, the influence of the primary particle structure should thus be considered. The correlation of the average crystallite size from Rietveld refinement (Figs. 3c and 3d) with the 1st cycle capacity loss is shown in Fig. 8b. Although an increase of the 1st cycle capacity loss with crystallite size is apparent, the rather weak correlation still allows for different interpretations. However, it again must be emphasized that the crystallite size only reflects an average over the whole sample powder, whereas in reality a distribution of primary particle sizes is present. A mere interpretation of size effects by PXRD refinement is therefore not sufficient. Even more importantly, the link between primary particles size and the accessible particles surfaces, *which evolve upon cycling*, must be addressed. A detailed study of the primary particle morphology and its impact on electrochemistry therefore will be part of an upcoming study.

Conclusions

Through the comparison of three methods with fundamentally different physical principles (X-ray diffraction, magnetism, electrochemical analysis), the validity of the generally applied structural model of LNO—the “off-stoichiometry model”—could be further reinforced. Within an industrially relevant parameter space for synthesis of polycrystalline LNO materials, the values of z in Li_{1-z}Ni_{1+z}O₂ were found to mainly depend on the Li excess applied in the calcination, whereas the calcination temperature mainly affected the average crystallite size. Besides PXRD being still the most robust technique for the determination of the crystallographic properties, the values of z are also correlated with magnetic properties, i.e. the Weiss constant, and with the half-cell potential of the H2–H3 phase transition, enabling an estimation of the stoichiometry by electrochemical measurements. However, it is pointed out that the absence of a sharp dQ/dV peak related to that phase transition does

not necessarily indicate the suppression of the phase transition, but can also be the result of sample inhomogeneity. Although being widely discussed in the literature, *no clear correlation* of a small Ni excess in the Li slab and the 1st cycle capacity loss was found for samples within an industrially reasonable physical parameter space.

Thus, we propose a correlation between the 1st cycle capacity loss and the different primary particle morphologies, as a (weak) correlation between 1st cycle reversibility and average crystallite size is present. Particle morphology has a direct impact on the surface area between cathode active material and electrolyte and is a key parameter to look at to understand the Li intercalation kinetics. However, a quantification of primary particle morphology is not a trivial task, as measuring a single value (average crystallite size) by PXRD is not sufficient and rather a distribution of particle sizes is needed. Moreover, the morphology will change during cycling due to fracturing of the secondary particle agglomerates, further complicating the task. Therefore, to further conclude the impact on the electrochemical performance, a detailed study on the primary particle morphology and its evolution upon cycling was performed and will be presented in a forthcoming publication.

Acknowledgments

The magnetization measurements were conducted at the Chair of Inorganic Chemistry with Focus on Novel Materials (Prof. Thomas Fässler) at the Technical University of Munich. François Fauth and the BL04-MSPD beamline team at the ALBA synchrotron are gratefully acknowledged for their support to the PXRD measurements.

ORCID

Philipp Kurzthals  <https://orcid.org/0000-0002-7013-080X>
 Felix Riewald  <https://orcid.org/0000-0001-9002-3633>
 Matteo Bianchini  <https://orcid.org/0000-0003-4034-7706>
 Hubert A. Gasteiger  <https://orcid.org/0000-0001-8199-8703>
 Jürgen Janek  <https://orcid.org/0000-0002-9221-4756>

References

1. A. Masias, J. Marcicki, and W. A. Paxton, *ACS Energy Lett.*, **6**, 621 (2021).
2. Y. Ding, Z. P. Cano, A. Yu, J. Lu, and Z. Chen, *Electrochemical Energy Reviews*, **2**, 1 (2019).
3. C. Xu, Q. Dai, L. Gaines, M. Hu, A. Tukker, and B. Steubing, *Communications Materials*, **1**, 99 (2020).
4. W. Li, E. M. Erickson, and A. Manthiram, *Nat. Energy*, **5**, 26 (2020).
5. L. Crogue and M. R. Palacin, *JACS*, **137**, 3140 (2015).
6. S.-T. Myung, F. Maglia, K.-J. Park, C. S. Yoon, P. Lamp, S.-J. Kim, and Y.-K. Sun, *ACS Energy Lett.*, **2**, 196 (2017).
7. D. Karabelli, S. Kiemel, S. Singh, J. Koller, S. Ehrenberger, R. Mieke, M. Weeber, and K. P. Birke, *frontiers in Energy Research*, **8**, 1 (2021).
8. J.-H. Kim, H.-H. Ryu, S. J. Kim, C. S. Yoon, and Y.-K. Sun, *ACS Appl. Mater. Interfaces*, **11**, 30936 (2019).
9. H.-J. Noh, S. Youn, C. S. Yoon, and Y.-K. Sun, *J. Power Sources*, **233**, 121 (2013).
10. A. O. Kondrakov, H. Geßwein, K. Galdina, L. De Biasi, V. Meded, E. O. Filatova, G. Schumacher, W. Wenzel, P. Hartmann, and T. Brezesinski, *The Journal of Physical Chemistry C*, **121**, 24381 (2017).
11. A. O. Kondrakov, A. Schmidt, J. Xu, H. Geßwein, R. Mönig, P. Hartmann, H. Sommer, T. Brezesinski, and J. R. Janek, *The Journal of Physical Chemistry C*, **121**, 3286 (2017).
12. L. de Biasi, A. Schiele, M. Roca-Ayats, G. Garcia, T. Brezesinski, P. Hartmann, and J. Janek, *ChemSusChem*, **12**, 2240 (2019).
13. R. Jung, M. Metzger, F. Maglia, C. Stinner, and H. A. Gasteiger, *J. Electrochem. Soc.*, **164**, A1361 (2017).
14. W. Yan, S. Yang, Y. Huang, Y. Yang, and Y. Guohui, *J. Alloys Compd.*, **819**, 153048 (2020).
15. L. Mu, W. H. Kan, C. Kuai, Z. Yang, L. Li, C.-J. Sun, S. Sainio, M. Avdeev, D. Nordlund, and F. Lin, *ACS Appl. Mater. Interfaces*, **12**, 12874 (2020).
16. L. Mu et al., *Chem. Mater.*, **31**, 9769 (2019).
17. K. Min, K. Park, S. Y. Park, S.-W. Seo, B. Choi, and E. Cho, *J. Electrochem. Soc.*, **165**, A79 (2018).
18. J.-M. Kim, X. Zhang, J.-G. Zhang, A. Manthiram, Y. S. Meng, and W. Xu, *Mater. Today*, **46**, 155 (2021).
19. J. Langdon and A. Manthiram, *Energy Storage Mater.*, **37**, 143 (2021).
20. J.-Y. Hwang, S.-M. Oh, S.-T. Myung, K. Y. Chung, I. Belharouak, and Y.-K. Sun, *Nat. Commun.*, **6**, 6865 (2015).
21. U. H. Kim, H. H. Ryu, J. H. Kim, R. Mücke, P. Kaghazchi, C. S. Yoon, and Y. K. Sun, *Adv. Energy Mater.*, **9**, 1803902 (2019).

22. H. H. Sun, H.-H. Ryu, U.-H. Kim, J. A. Weeks, A. Heller, Y.-K. Sun, and C. B. Mullins, *ACS Energy Lett.*, **5**, 1136 (2020).
23. S.-H. Kang, W.-S. Yoon, K.-W. Nam, X.-Q. Yang, and D. P. Abraham, *J. Mater. Sci.*, **43**, 4701 (2008).
24. M. D. Radin, S. Hy, M. Sina, C. Fang, H. Liu, J. Vinckeviciute, M. Zhang, M. S. Whittingham, Y. S. Meng, and A. Van der Ven, *Adv. Energy Mater.*, **7**, 1602888 (2017).
25. J. Kasnatscheew, M. Evertz, B. Streipert, R. Wagner, R. Klöpsch, B. Vortmann, H. Hahn, S. Nowak, M. Amereller, and A.-C. Gentschev, *Phys. Chem. Chem. Phys.*, **18**, 3956 (2016).
26. H. Zhou, F. Xin, B. Pei, and M. S. Whittingham, *ACS Energy Lett.*, **4**, 1902 (2019).
27. R. Kanno, H. Kubo, Y. Kawamoto, T. Kamiyama, F. Izumi, Y. Takeda, and M. Takano, *J. Solid State Chem.*, **110**, 216 (1994).
28. W. Li, J. Reimers, and J. Dahn, *Physical Review B*, **46**, 3236 (1992).
29. A. Hirano, R. Kanno, Y. Kawamoto, Y. Takeda, K. Yamaura, M. Takano, K. Ohyama, M. Ohashi, and Y. Yamaguchi, *Solid State Ionics*, **78**, 123 (1995).
30. M. Bianchini, M. Roca-Ayats, P. Hartmann, T. Brezesinski, and J. Janek, *Angew. Chem. Int. Ed.*, **58**, 10434 (2019).
31. H. Arai, S. Okada, H. Ohtsuka, M. Ichimura, and J. Yamaki, *Solid State Ionics*, **80**, 261 (1995).
32. C. Delmas, J. P. Pérès, A. Rougier, A. Demourgues, F. Weill, A. Chadwick, M. Broussely, F. Perton, P. Biensan, and P. Willmann, *J. Power Sources*, **68**, 120 (1997).
33. V. Bianchi, S. Bach, C. Belhomme, J. Farcy, J. P. Pereira-Ramos, D. Caurant, N. Baffier, and P. Willmann, *Electrochim. Acta*, **46**, 999 (2001).
34. A. Rougier, P. Gravereau, and C. Delmas, *J. Electrochem. Soc.*, **143**, 1168 (1996).
35. R. V. Moshtev, P. Zlatilova, V. Manev, and A. Sato, *J. Power Sources*, **54**, 329 (1995).
36. V. Bianchi, D. Caurant, N. Baffier, C. Belhomme, E. Chappel, G. Chouteau, S. Bach, J. P. Pereira-Ramos, A. Sulpice, and P. Willmann, *Solid State Ionics*, **140**, 1 (2001).
37. F. Fauth, I. Peral, C. Popescu, and M. Knapp, *Powder Diffr.*, **28**, S360 (2013).
38. J. Rodríguez-Carvajal, *Physica B*, **192**, 55 (1993).
39. T. Roisnel and J. Rodríguez-Carvajal, *Mater. Sci. Forum*, **378–381**, 118 (2001).
40. T. Ohzuku, A. Ueda, and M. Nagayama, *J. Electrochem. Soc.*, **140**, 1862 (1993).
41. J. Rodríguez-Carvajal, *Study of Micro-Structural Effects by Powder Diffraction Using the Program FULLPROF*, Laboratoire Léon Brillouin (CEA-CNRS) (2003), https://cdifx.univ-rennes1.fr/fps/Microstructural_effects.pdf.
42. L. Yin, G. S. Mattei, Z. Li, J. Zheng, W. Zhao, F. Omenya, C. Fang, W. Li, J. Li, and Q. Xie, *Rev. Sci. Instrum.*, **89**, 093002 (2018).
43. G. A. Bain and J. F. Berry, *J. Chem. Educ.*, **85**, 532 (2008).
44. L. D. Dyer, B. S. Borie Jr, and G. P. Smith, *JACS*, **76**, 1499 (1954).
45. J. B. Goodenough, D. G. Wickham, and W. J. Croft, *J. Phys. Chem. Solids*, **5**, 107 (1958).
46. R. D. Shannon, *Acta crystallographica Section A: Crystal Physics, Diffraction, Theoretical and General Crystallography*, **32**, 751 (1976).
47. M. Bianchini, F. Fauth, P. Hartmann, T. Brezesinski, and J. Janek, *J. Mater. Chem. A*, **8**, 1808 (2020).
48. M. Bianchini et al., *Chem. Mater.*, **32**, 9211 (2020).
49. H. S. Liu, Z. R. Zhang, Z. L. Gong, and Y. Yang, *Electrochem. Solid-State Lett.*, **7**, A190 (2004).
50. D.-H. Cho, C.-H. Jo, W. Cho, Y.-J. Kim, H. Yashiro, Y.-K. Sun, and S.-T. Myung, *J. Electrochem. Soc.*, **161**, A920 (2014).
51. D. Pritzl, T. Teufl, A. T. S. Freiberg, B. Strehle, J. Sicklinger, H. Sommer, P. Hartmann, and H. A. Gasteiger, *J. Electrochem. Soc.*, **166**, A4056 (2019).
52. Y. Kim, H. Park, J. H. Warner, and A. Manthiram, *ACS Energy Lett.*, **6**, 941 (2021).
53. S. Ahmed et al., *ACS Nano*, **13**, 10694 (2019).
54. E. McCalla, G. H. Carey, and J. R. Dahn, *Solid State Ionics*, **219**, 11 (2012).
55. T. Sata, *Ceram. Int.*, **24**, 53 (1998).
56. H. Beyer, S. Meini, N. Tsiouvaras, M. Piana, and H. Gasteiger, *Phys. Chem. Chem. Phys.*, **15**, 11025 (2013).
57. H. Arai, S. Okada, Y. Sakurai, and J.-i. Yamaki, *Solid State Ionics*, **95**, 275 (1997).
58. R. M. German, *Crit. Rev. Solid State Mater. Sci.*, **35**, 263 (2010).
59. J. Zheng, P. Yan, L. Estevez, C. Wang, and J.-G. Zhang, *Nano Energy*, **49**, 538 (2018).
60. H. Ronduda, M. Zybort, A. Szczęśna-Chrzan, T. Trzeciak, A. Ostrowski, D. Szymański, W. Wiczeorek, W. Raróg-Pilecka, and M. Marcinek, *Nanomaterials*, **10**, 2018 (2020).
61. J. Zhu and G. Chen, *J. Mater. Chem. A*, **7**, 5463 (2019).
62. J. Li, H. Li, W. Stone, R. Weber, S. Hy, and J. R. Dahn, *J. Electrochem. Soc.*, **164**, A3529 (2017).
63. S.-Y. Lee, G.-S. Park, C. Jung, D.-S. Ko, S.-Y. Park, H. G. Kim, S.-H. Hong, Y. Zhu, and M. Kim, *Adv. Sci.*, **6**, 1800843 (2019).
64. S. Permin, T. Neumann, S. Indris, G. Neubüser, L. Kienle, A. Fiedler, A.-L. Hansen, D. Gianolio, T. Bredow, and W. Bensch, *Phys. Chem. Chem. Phys.*, **20**, 19129 (2018).
65. L. Vegard, *Z. Phys.*, **5**, 17 (1921).
66. L. Yin, Z. Li, G. S. Mattei, J. Zheng, W. Zhao, F. Omenya, C. Fang, W. Li, J. Li, and Q. Xie, *Chem. Mater.*, **32**, 1002 (2019).
67. C. Poullierie, E. Suard, and C. Delmas, *J. Solid State Chem.*, **158**, 187 (2001).
68. A. Mesnier and A. Manthiram, *ACS Appl. Mater. Interfaces*, **12**, 52826 (2020).
69. W. Hu, H. Wang, W. Luo, B. Xu, and C. Ouyang, *Solid State Ionics*, **347**, 115257 (2020).
70. F. Kong, C. Liang, L. Wang, Y. Zheng, S. Peranathan, R. C. Longo, J. P. Ferraris, M. Kim, and K. Cho, *Adv. Energy Mater.*, **9**, 1802586 (2019).
71. A. Rougier, C. Delmas, and A. V. Chadwick, *Solid State Commun.*, **94**, 123 (1995).
72. P. W. Anderson, *Mater. Res. Bull.*, **8**, 153 (1973).
73. K. Hirakawa, H. Kadowaki, and K. Ubukoshi, *J. Phys. Soc. Jpn.*, **54**, 3526 (1985).
74. J. P. Kemp, P. A. Cox, and J. W. Hodby, *J. Phys. Condens. Matter*, **2**, 6699 (1990).
75. K. Hirota, Y. Nakazawa, and M. Ishikawa, *J. Phys. Condens. Matter*, **3**, 4721 (1991).
76. A. Rougier, C. Delmas, and G. Chouteau, *J. Phys. Chem. Solids*, **57**, 1101 (1996).
77. K. Yamaura, M. Takano, A. Hirano, and R. Kanno, *J. Solid State Chem.*, **127**, 109 (1996).
78. E. Chappel, M. D. Núñez-Regueiro, G. Chouteau, O. Isnard, and C. Darie, *The European Physical Journal B - Condensed Matter and Complex Systems*, **17**, 615 (2000).
79. M. D. Radin and A. Van der Ven, *Chem. Mater.*, **30**, 607 (2018).
80. G. Klinser, S. Topolovec, H. Krenn, and R. Würschum, *Encyclopedia of Interfacial Chemistry*, ed. K. Wandelt (Elsevier, Amsterdam: Oxford) 849 (2018).
81. Y. Hu, G. Z. Iwata, M. Mohammadi, E. V. Sillelta, A. Wickenbrock, J. W. Blanchard, D. Budker, and A. Jerschow, *Proc. Natl. Acad. Sci.*, **117**, 10667 (2020).
82. C. Delmas, M. Ménétrier, L. Croguennec, S. Levasseur, J. P. Pérès, C. Poullierie, G. Prado, L. Fournès, and F. Weill, *Int. J. Inorg. Mater.*, **1**, 11 (1999).
83. W. Li, J. N. Reimers, and J. R. Dahn, *Solid State Ionics*, **67**, 123 (1993).
84. J. R. Dahn, U. von Sacken, and C. A. Michal, *Solid State Ionics*, **44**, 87 (1990).
85. E. Levi, M. D. Levi, G. Salitra, D. Aurbach, R. Oesten, U. Heider, and L. Heider, *Solid State Ionics*, **126**, 97 (1999).
86. X. Q. Yang, X. Sun, and J. McBreen, *Electrochem. Commun.*, **1**, 227 (1999).
87. H. Li, N. Zhang, J. Li, and J. Dahn, *J. Electrochem. Soc.*, **165**, A2985 (2018).
88. M. Mock, M. Bianchini, S. Siculo, F. Fauth, and K. Albe, *J. Mater. Chem. A*, **9**, 14928 (2021).
89. J. P. Peres, F. Weill, and C. Delmas, *Solid State Ionics*, **116**, 19 (1999).
90. M. E. Arroyo y de Dompablo, A. Van der Ven, and G. Ceder, *Physical Review B*, **66**, 064112 (2002).
91. A. Aishova, G.-T. Park, C. S. Yoon, and Y.-K. Sun, *Adv. Energy Mater.*, **10**, 1903179 (2020).
92. H.-H. Ryu, G.-T. Park, C. S. Yoon, and Y.-K. Sun, *J. Mater. Chem. A*, **7**, 18580 (2019).
93. J. Park et al., *Nat. Mater.*, **20**, 991 (2021).
94. C. Heubner, T. Liebmann, M. Schneider, and A. Michaelis, *Electrochim. Acta*, **269**, 745 (2018).
95. T. Liebmann, C. Heubner, C. Lämmel, M. Schneider, and A. Michaelis, *ChemElectroChem*, **6**, 5728 (2019).
96. J. K. A. Park, S.-Y. Han, J. Paulsen, K.-T. Lee, and R. De Palma, *Precursor And Method For Preparing Ni Based Cathode Material For Rechargeable Lithium Ion Batteries*, WO/2018/158078 (2018).
97. L. Croguennec, E. Suard, P. Willmann, and C. Delmas, *Chem. Mater.*, **14**, 2149 (2002).
98. R. Ruess, S. Schweidler, H. Hemmelmann, G. Conforto, A. Bielefeld, D. A. Weber, J. Sann, M. T. Elm, and J. Janek, *J. Electrochem. Soc.*, **167**, 100532 (2020).
99. A. Grenier, P. J. Reeves, H. Liu, I. D. Seymour, K. Märker, K. M. Wiaderek, P. J. Chupas, C. P. Grey, and K. W. Chapman, *JACS*, **142**, 7001 (2020).